Journal of Materials Chemistry A

ROYAL SOCIETY OF CHEMISTRY

PAPER

View Article Online
View Journal | View Issue

Cite this: J. Mater. Chem. A, 2022, 10, 18322

Oxygen defect engineering endows Co_3O_4 nanosheets with advanced aluminum ion storage†

Jiening Zheng,‡ Tian Xu,‡ Guanglin Xia and Xuebin Yu *

Received 24th May 2022
Accepted 12th August 2022

DOI: 10.1039/d2ta04165k

rsc.li/materials-a

Atomic-level structure modulation is an effective way to boost ionic diffusion kinetics and improve the cycling stability. To relieve the strong coulombic ion–lattice interactions originating from trivalent Al^{3+} ions, herein oxygen-deficient Co_3O_{4-x} porous nanosheets are fabricated *via* a facile $NaBH_4$ reduction strategy using a metal–organic framework template. Electrochemical kinetics analysis and theoretical calculation results reveal good pseudocapacitive property, appropriate diffusion capability and Al^{3+} formation energy, corroborating fast Al^{3+} ion storage/release kinetics and high Al^{3+} storage capacity. Specifically, Co_3O_{4-x} porous nanosheets exhibit a high reversible capacity of 442.3 mA h g^{-1} at 1.0 A g^{-1} and retain 104.2 mA h g^{-1} after 1800 cycles, remarkably higher than those of the previously reported Co_3O_4-based cathode materials. Furthermore, *ex situ* analyses reveal the conversion reaction mechanism of the Co_3O_{4-x} cathode, followed by its high structural stability upon extended cycling.

Introduction

Lithium-ion batteries (LIBs) have dominated in the energy storage market for smart vehicles and portable electronic devices due to their long-term cycling durability and high energy density; however, the limited lithium resources and safety concerns hinder their development in large-scale energy storage.[1–4] An effective solution to solve these problems is to develop potent candidates with low cost and high energy density. Among the beyond Li-ion technologies, the aluminum metal anode, as a three-charge carrier, offers a gravimetric capacity (2980 mA h g^{-1}) comparable to that of the Li anode and ultra-high volumetric capacity (8040 mA h cm^{-3}).[5] Also, Al is a naturally abundant element and safe to handle owing to its inert nature when exposed to air. In 2015, Dai *et al.* made a breakthrough in aluminium-ion batteries (AIBs) in terms of cycling stability and rate capability using a graphitic foam cathode and a chloroaluminate ionic liquid electrolyte.[6] From then on, various kinds of carbon-based cathodes, such as carbon nanoscrolls,[7] graphitic,[8,9] graphene,[10–13] and so on, have been developed as promising AIB cathodes due to their attractive electrochemical performance, especially the excellent long-term stability, superior rate capability, and high discharge plateau. However, $AlCl_4^-$ intercalation/deintercalation leads to limited capacities of these cathode materials due to the monovalent $AlCl_4^-$ storage properties. Moreover, the $AlCl_4^-$ storage reaction operates at the expense of the electrolyte, which is unfavorable for energy density improvement as the electrolyte amount is a key factor for high energy density.[14] Alternatively, another category of AIB cathodes based on trivalent Al^{3+} ions as the intercalation/conversion reagent have been regarded as promising candidates for AIBs owing to their desirable capacity. The cathode materials used for this category of AIBs mainly include metal oxides, chalcogenides and phosphides.[15–17] Metal oxides have been extensively explored as promising electrode materials for advanced secondary batteries owing to their high theoretical capacity and low cost.[18–21] Among the numerous candidates, Co_3O_4 has attracted particular attention due to its high theoretical specific capacity, stable chemical properties and wide availability.[22–25] Unsurprisingly, the initial discharge capacity of Co_3O_4 based cathodes can easily reach 250–500 mA h g^{-1}; however, they always suffer from limited cycles and poor rate performance, which can be ascribed to the intrinsic limitation related to the intercalation chemistry of trivalent Al^{3+}.[15] Given the high electronegativity of oxygen and the large charge density of Al^{3+}, the resulting strong coulombic ion–lattice interactions can cause clumsy Al^{3+} diffusion and inhibit reversible Al^{3+} intercalation.[26,27] Therefore, it is necessary to develop an efficient strategy to favor Al^{3+} diffusion and reversible Al^{3+} intercalation/deintercalation in Co_3O_4 based cathode materials.

Valence engineering (vacancy, doping, *etc.*) refers to modifying the electronic structure of materials, which can effectively improve the electrochemical performance of the electrode materials.[28,29] Oxygen defects can act as an electronic charge carrier to greatly enhance the electrical conductivity, which have been widely used in the modification of electrode materials.[30] In addition, the Gibbs free energy of metal ion adsorption on the

Department of Materials Science, Fudan University, Shanghai 200433, China. E-mail: yuxuebin@fudan.edu.cn

† Electronic supplementary information (ESI) available. See https://doi.org/10.1039/d2ta04165k

‡ Jiening Zheng and Tian Xu contributed equally to this work.

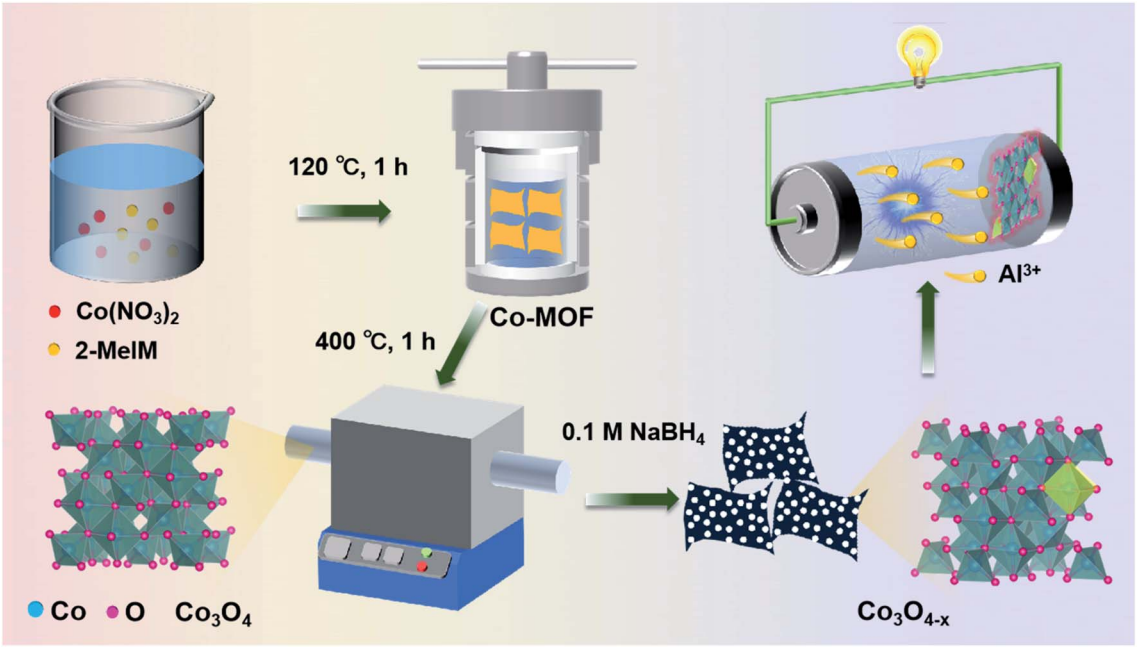

Fig. 1 Schematic strategy for the synthesis of Co_3O_{4-x}.

surface of the material can be modified by the oxygen defects, which is important to provide an estimation of the ease of ion adsorption/desorption, *i.e.*, reversibility. Furthermore, oxygen defects can release excess electrons around the oxygen vacancies, which could be treated as electron donors to attract cations and promote fast cation diffusion kinetics.[28,31] Therefore, introducing oxygen defects into Co_3O_4 to adjust its electronic structure would be expected to achieve high-performance Al^{3+} storage behavior.

Herein, by employing ultrathin metal–organic-framework (MOF) nanosheets as precursors and templates, we construct oxygen-deficient porous Co_3O_4 nanosheets in the form of interconnected nanoparticles embedded in the MOF nanosheet derived carbon substrate *via* an *in situ* oxidation reaction and $NaBH_4$ treatment. Electrochemical performance and theoretical simulations demonstrate that the partial extraction of electronegative oxygen from the Co_3O_4 lattice is effective for facilitating the reversibility of Al^{3+} storage/release. Besides, the large-surface-area ultrathin interwoven porous structure can greatly shorten the Al^{3+} diffusion path and increase the electrolyte infiltration area, further improving the Al^{3+} diffusion and storage capacity. The resulting cathode displays high capacity (442.3 mA h g^{-1}) and long-term cyclability (up to 1800 cycles) with average coulombic efficiency (CE) > 97%, making it a promising candidate for high-performance AIBs.

Results and discussion

The successful preparation of Co_3O_{4-x} porous nanosheets involves three steps, and the schematic illustration is shown in Fig. 1: (1) the solvothermal synthesis of cobalt-based metal–organic-framework (Co-MOF) nanosheets, (2) the subsequent thermal self-template conversion of Co-MOF precursors into Co_3O_4 porous nanosheets at 400 °C in air, and (3) the 0.1 M $NaBH_4$ reduction transformation of Co_3O_4 nanosheets into Co_3O_{4-x} nanosheets. Fig. 2a and b display the scanning electron microscopy (SEM) images of the precursor Co-MOF, in which thin and wrinkled nanosheets with smooth surfaces are observed, indicating their high elasticity and flexibility. Besides, its corresponding X-ray powder diffraction (XRD) pattern is given in Fig. S1.† After air calcination, the smooth surface disappeared and a large number of nanoscale pores appeared throughout the nanosheets (Fig. 2c and d), forming an interwoven holey structure. Such multi-holey channels can not only facilitate electrolyte permeation, but also effectively shorten the ion transport distance. Co_3O_{4-x} porous nanosheets were obtained *via* $NaBH_4$ reduction, and present a similar interwoven holey nanosheet shape as shown in SEM (Fig. 2e and f) and transmission electron microscopy (TEM, Fig. 2g) images. The interlayer spacings of 0.47 and 0.29 nm (Fig. 2i) correspond to the (111) and (220) planes of Co_3O_4 (JCPDS No. 42–1467), respectively. In addition, some obvious lattice distortion and vacancies can be found due to the existence of abundant oxygen defects resulting from the $NaBH_4$ reduction (Fig. 2h).[32] The corresponding selected area electron diffraction (SAED) pattern reveals the single-crystalline nature of Co_3O_{4-x} (inset in Fig. 2i). Scanning TEM with energy dispersive X-ray spectroscopy (STEM-EDX) elemental mapping images confirm the homogeneous distribution of Co and O in the Co_3O_{4-x} porous nanosheets (Fig. 2j). Besides, the TEM and elemental mapping images of Co_3O_4 are given in Fig. S2,† and they exhibit similar morphology with uniform elemental distribution. In addition, when subjected to high temperature (400 °C) air annealing, the carbon species can be oxidized to CO_2,[33] resulting in composites

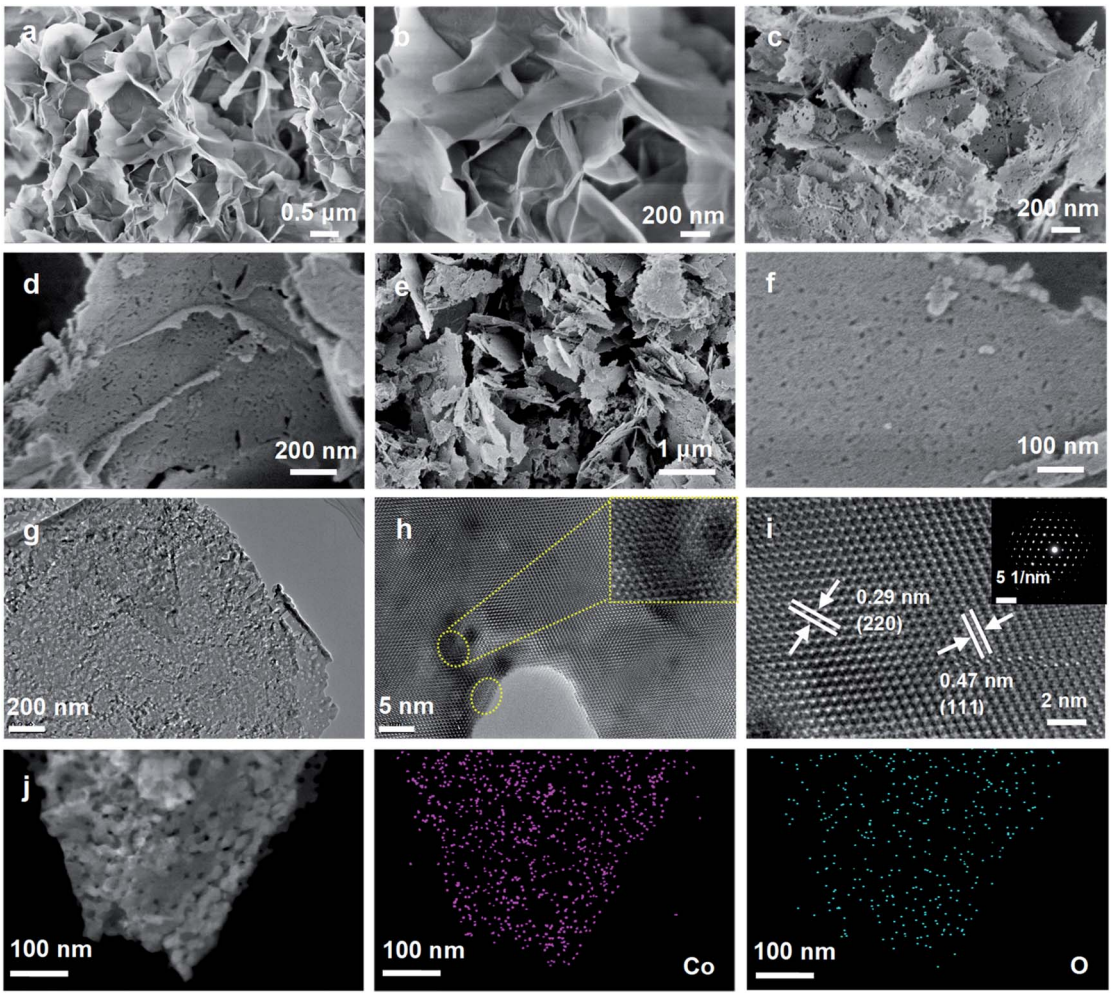

Fig. 2 (a and b) SEM images of Co-MOF. (c and d) SEM images of Co_3O_4. (e and f) SEM, (g) TEM, and (h and i) HRTEM images and SAED pattern (inset in i) for Co_3O_{4-x}. (j) STEM-EDX elemental mapping images of Co_3O_{4-x}.

with ultra-low carbon content confirmed by the EDX elemental mapping image (Fig. S3†) and EDX pattern (Fig. S4†). The Brunauer–Emmett–Teller (BET) surface areas and pore size distributions of Co_3O_{4-x} and Co_3O_4 porous nanosheets were measured from N_2 adsorption–desorption isotherms. The BET surface areas were found to be up to 51.0 and 36.7 $m^2\ g^{-1}$ for Co_3O_{4-x} and Co_3O_4 porous nanosheets (Fig. S5a†), respectively, revealing that oxygen defects could increase the BET surface area.[34] Both Co_3O_{4-x} and Co_3O_4 nanosheets are mesoporous structures with pore size distributions from 2 to 15 nm and 2 to 10 nm (Fig. S5b†), respectively, which are consistent with the SEM and TEM observations. The mesoporous structure of these composites enables fast electrolyte penetration in the electrodes.[35]

The crystal structures of Co_3O_{4-x} and Co_3O_4 porous nanosheets were obtained from X-ray powder diffraction (XRD). As displayed in Fig. 3a, both samples have the same crystal structure, and the diffraction peaks are well indexed to Co_3O_4 (JCPDS No. 42–1467). Meanwhile, Co_3O_{4-x} nanosheets exhibit weaker and broader diffraction peaks, suggesting their low crystallinity originating from oxygen defects after $NaBH_4$ treatment.[36] The oxygen-deficient structure of Co_3O_{4-x} nanosheets was confirmed by X-ray photoelectron spectroscopy (XPS), Raman spectra, and electron paramagnetic resonance (EPR). XPS survey spectra signify the coexistence of Co and O elements in both samples (Fig. 3b). The high-resolution spectrum of Co 2p (Fig. 3c) shows two major peaks at around 779 (Co $2p_{3/2}$) and 794 eV (Co $2p_{1/2}$), and each peak can be divided into two mixed contributions of Co^{3+} and Co^{2+}, respectively. Notably, the surface ratio of Co^{3+}/Co^{2+} is 1.25 for Co_3O_{4-x} nanosheets, obviously lower than that of Co_3O_4 nanosheets (1.49), verifying the presence of oxygen vacancies which are balanced by the conversion of Co^{3+} to Co^{2+} in the Co_3O_{4-x} nanosheets.[37] Meanwhile, the XPS O 1 s spectrum intuitively displays an enrichment of oxygen-vacancy on the surface of Co_3O_{4-x} porous nanosheets (Fig. 3d).[38] The slight blue shift (5.2 cm^{-1}) of the Raman band at 669.1 cm^{-1} for Co_3O_{4-x} nanosheets compared with that of Co_3O_4 nanosheets also suggests the formation of oxygen vacancies (Fig. 3e).[32] In addition, Co_3O_{4-x} shows an intensive EPR signal at $g = 2.006$, which further provides the direct evidence for oxygen vacancies in this sample (Fig. 3f).[39]

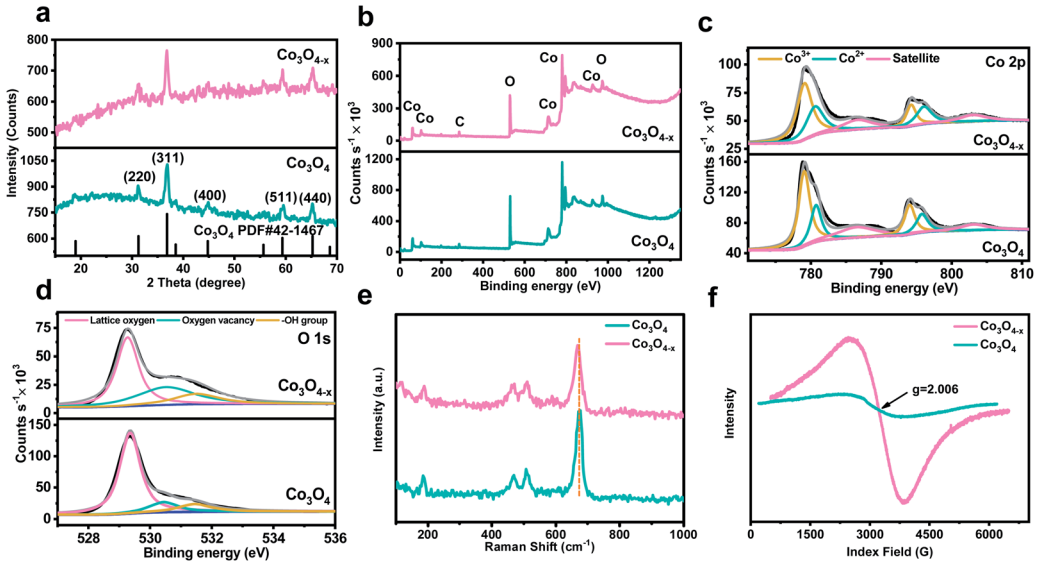

Fig. 3 (a) XRD patterns of Co_3O_{4-x} and Co_3O_4. (b) The integrated XPS spectra of Co_3O_{4-x} and Co_3O_4 and the high-resolution XPS of (c) Co 2p, (d) O 1 s for Co_3O_{4-x} and Co_3O_4. (e) Raman and (f) EPR spectra of Co_3O_{4-x} and Co_3O_4.

To explore the function of the oxygen-deficient structure in Al^{3+} storage processes, the electrochemical performance was investigated in a Swagelok-type cell composed of a Co_3O_4 based composite cathode, Al foil anode, and a paper glass fiber separator infiltrated with an ionic liquid electrolyte. The cyclic voltammograms (CV) of Co_3O_{4-x} nanosheets between 0.01 and 2.25 V at 1.0 mV s^{-1} display three pairs of redox peaks at around 2.11/1.74 V, 1.10/1.05 V, and 0.39/0.28 V (Fig. 4a), due to the intercalation/deintercalation of Al^{3+} in the Co_3O_{4-x} porous nanosheets. Compared with the CV curve of Co_3O_4 nanosheets (Fig. S6†), the Co_3O_{4-x} nanosheets present higher peak current densities, indicating that Co_3O_{4-x} nanosheets exhibit improved Al^{3+} storage/release ability. The galvanostatic charge/discharge profiles of Co_3O_{4-x} nanosheets are given in Fig. 4b, in which a high initial discharge capacity of 442.3 mA h g^{-1} achieved at 1.0 A g^{-1} can be observed. Notably, the voltage profile shows reduced polarization as well as extended plateaus with cycling, revealing the activation process of Co_3O_{4-x} nanosheets. In contrast, the Co_3O_4 porous nanosheets exhibit low initial discharge capacity (265.7 mA h g^{-1}, 1.0 A g^{-1}), large polarization, and relatively short plateaus (Fig. 4c). These results illustrate that the Co_3O_{4-x} nanosheets with O vacancies enable high active material utilization and effectively improve the reaction kinetics. The rate capabilities of the two samples were evaluated at various current densities from 0.5 to 5.0 A g^{-1} (Fig. 4d). Notably, the Co_3O_{4-x} porous nanosheets deliver impressive reversible specific capacities of 512.5, 405.7, 232.23, 137.2, and 58.6 mA h g^{-1} at current densities of 0.5, 1.0, 2.0, 3.0, and 5.0 A g^{-1}, respectively, whereas the specific capacities of Co_3O_4 nanosheets are only 357.4, 224.3, 95.8, 51.6, and 36.7 mA h g^{-1} at the same current densities. When the current density returned to 0.5 A g^{-1}, the specific capacity of the Co_3O_{4-x} nanosheets recovered to 550.9 mA h g^{-1}. These results suggest that the O vacancies can significantly improve the rate performance of the Co_3O_{4-x} porous nanosheet cathode, attributed to the intrinsic enhanced ion diffusion kinetics.[40,41] Interestingly, the coulombic efficiency is over 100% at the recovered current density of 0.5 A g^{-1}, which could be explained as follows. Due to the high electronegativity of oxygen and the large charge density of Al^{3+}, the generated strong coulombic ion–lattice interactions can induce the trapping of some Al^{3+} in the host lattice during the repeated discharge/charge process, thereby preventing Al^{3+} release upon charging.[42] This phenomenon can be confirmed from the low coulombic efficiencies in the initial rate cycling process. However, the recovered low charge–discharge current density of 0.5 A g^{-1} is conducive to inducing gradual reactivation of the previously trapped Al^{3+} during the charging process, resulting in greater charging capacities than discharging capacities (coulombic efficiencies > 100%).[42] A similar phenomenon could be observed in a previously reported AIB cathode.[14] Moreover, the galvanostatic charge/discharge profiles at various rates exhibit similar shapes and deliver distinct plateaus even at high current densities, reflecting the high charge-transfer kinetics of Co_3O_{4-x} nanosheets (Fig. 4e). It is wellknown that the structure of electrode materials can be subjected to damage at large current densities, leading to fast capacity loss. Thus, the high-rate cycling process is also significant for practical application.[43] As shown in Fig. 4f, the Al^{3+} intercalation/deintercalation plateaus still exist after ultra-long 1800 cycles performed at 1 A g^{-1}, reflecting the high structural stability of Co_3O_{4-x} nanosheets. The detailed cycling performances and corresponding coulombic efficiencies at 1 A g^{-1} for Co_3O_{4-x} and Co_3O_4 are presented in Fig. 4g. The discharge capacity of Co_3O_{4-x} decreases in the initial 100 cycles and stays relatively steady in the following cycles. Specifically, a specific capacity of 123.6 mA h g^{-1} was retained after 1000 cycles. Prolonging the cycling up to 1800 cycles still affords a reversible capacity of

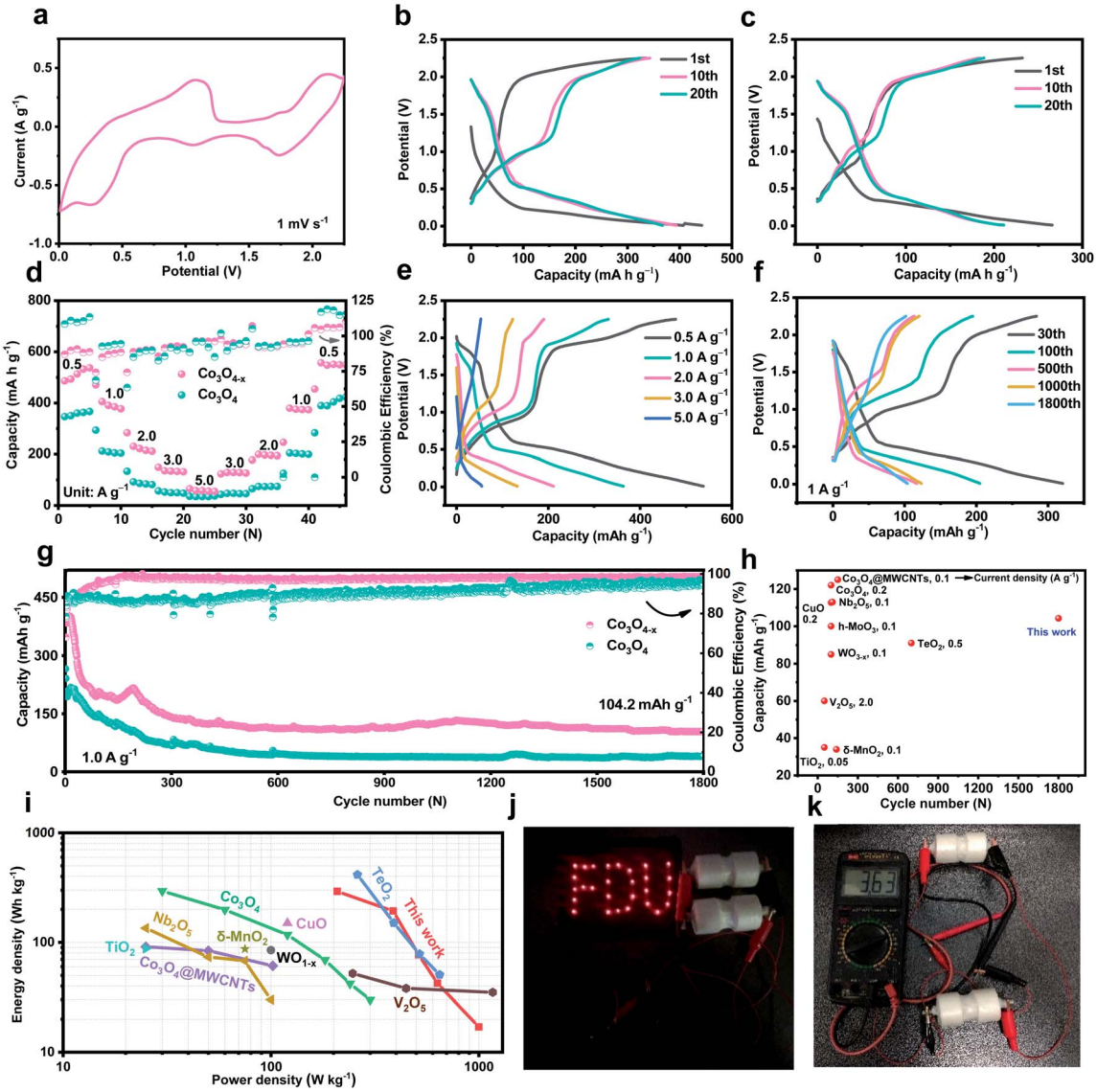

Fig. 4 (a) CV curve of Co_3O_{4-x} obtained at a scanning rate of 1.0 mV s^{-1}. The selected galvanostatic discharge–charge profiles of (b) Co_3O_{4-x} and (c) Co_3O_4 at 1000 mA g^{-1}. (d) The rate capabilities and corresponding coulombic efficiencies of Co_3O_{4-x} and Co_3O_4 at current densities from 0.5 to 5.0 A g^{-1}. (e) Galvanostatic discharge–charge profiles of Co_3O_{4-x} at different current densities. (f) The selected galvanostatic discharge–charge profiles of Co_3O_{4-x} during the cycling test. (g) Cycling performance of Co_3O_{4-x} and Co_3O_4 at 1000 mA g^{-1}. (h) Electrochemical performance comparison with the reported oxide-based AIB cathodes. (i) Ragone plots of Co_3O_{4-x} and the previously reported oxide-based cathodes. (j) Two serially connected Co_3O_{4-x}/Al batteries for powering 28 LEDs and (k) the measured total voltage.

104.2 mA h g^{-1} with steady coulombic efficiency close to 99%, nearly 2.6 times higher than that of Co_3O_4 nanosheets. The discharge capacity decreases in the initial cycles which could be attributed to the formation of a solid electrolyte interphase (SEI) layer, electrolyte decomposition, and side reactions.[16,44–46] These results are competitive among the reported oxide cathodes for AIBs shown in Fig. 4h and Table S1,†[23,47–55] strongly supporting the intriguing structural superiorities of Co_3O_{4-x} porous nanosheets as an advanced cathode for AIBs. The corresponding Ragone plot in Fig. 4i shows that Co_3O_{4-x} can deliver a high energy density of 292.1 W h kg^{-1} (based on the cathode mass) and power density of 1000 W kg^{-1}, which are superior or comparable to those of previously reported oxide-based AIB cathodes.[23,47–54] In addition, to demonstrate the practical application potential of the Co_3O_{4-x}/Al battery, both our fabricated Co_3O_{4-x}/Al batteries were connected in series, which could easily light up 28 light emitting diode (LED) lamps (Fig. 4j), and the voltage of the batteries in series could reach 3.63 V (Fig. 4k). Moreover, these two series-wound Co_3O_{4-x}/Al batteries could be employed to light a 3 V LED lamp for more than a week (Fig. S7†), further indicating the practical application prospects. Besides, we also checked the Al^{3+} storage performance of the precursor Co-MOF within the same potential window of 0.01–2.25 V at 1 A g^{-1}. As shown in Fig. S8a and b,† the Co-MOF exhibits larger polarization, poor cycling

stability, low capacity, and unsatisfactory average CE, suggesting its inferior performance towards Al^{3+} storage.

We further inquired into the Al^{3+} storage mechanism in the electrochemical cycling process of Co_3O_{4-x} nanosheets using *ex situ* XPS characterizations. Different terminated voltage stages in the discharge–charge process were monitored (Fig. 5a). The changes of Co 2p and Al 2p XPS spectra at the different stages are displayed in Fig. 5b and c, respectively. To reduce the adsorbed electrolyte effects, the XPS spectra are obtained *via* argon etching. Specifically, as displayed in Fig. 5b, the pristine Co_3O_{4-x} cathode clearly shows three pairs (Co $2p_{1/2}$ and Co $2p_{3/2}$) of Co 2p peaks corresponding to the Co^{2+} ,Co^{3+} and satellite peaks. Two new peaks appear at 778.8 and 795.0 eV ascribed to Co^0 in the discharging process, accompanied by the gradual weakened Co^{3+} signals and the increased Co^{2+} signals. During the charging process, the valence sates of the cobalt species increase and recover to their original ones gradually. After fully charging to 2.25 V, Co 2p shows a similar spectrum to the original one. Meanwhile, the Al 2p intensity displays a pronounced increasing tendency in the discharging process, while the trend shows a sharp reversal in the charging process (Fig. 5c). In addition, the Al 2p peak in the fully discharged state is stronger than that in the fully charged state. These observations signify that Co^{3+} is reduced to a lower state with the Al^{3+} insertion and recovered with Al^{3+} reversible deinsertion in the following charging process. *Ex situ* XRD measurements were further performed to investigate the crystal structure changes of Co_3O_{4-x} porous nanosheets during the discharge–charge process. As shown in Fig. 5d, the (400) peak left shifts from about 44.7° to 44.0° after fully discharging, suggesting that the insertion of Al^{3+} induces larger interlayer space. In this process, the Co ions in Co_3O_{4-x} are partially substituted by Al^{3+}, resulting in $Al_lCo_mO_{4-x}$ and elemental Co.[49] When recharged to 2.25 V, the peak returns to the pristine position, indicating the good reversibility of the Al^{3+} intercalation/deintercalation process. The *ex situ* SEM and TEM images of Co_3O_{4-x} porous nanosheets at the discharged and charged states are illustrated in Fig. S9,† respectively. The porous nanosheet structure is retained in both discharged and charged states (Fig. S9a–c and e–g†). The HRTEM images and SAED patterns in Fig. S9d and h† reveal the robust structure of Co_3O_{4-x} porous nanosheets after the discharging and charging process, which are quite

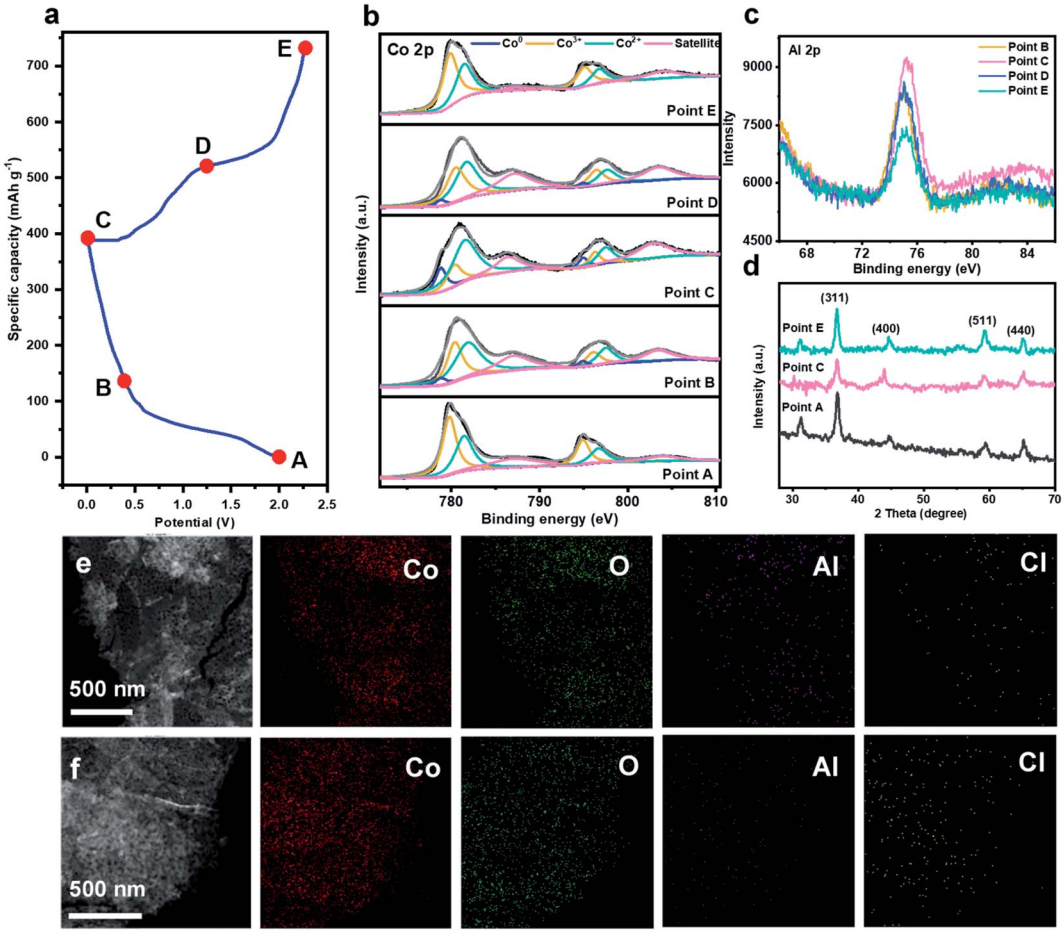

Fig. 5 (a) Charge–discharge curves of Co_3O_{4-x}. Five stages were monitored: the original state (point A), the state of discharge to 0.4 V (point B), the fully discharged state (point C), the state of charge to 1.25 V (point D), and the fully charged state (point E). *Ex situ* XPS data of the (b) Co 2p, (c) Al 2p peaks for Co_3O_{4-x} at the corresponding states. (d) *Ex situ* XRD patterns of Co_3O_{4-x} at the original, fully discharged, and fully charged states. STEM-EDX elemental mapping images of (e) fully discharged and (f) fully charged Co_3O_{4-x}.

consistent with the *ex situ* XRD patterns (Fig. 5d). Moreover, the STEM-EDX elemental mapping images reveal a much higher Al content in the discharged state (Fig. 5e) compared with that in the charged state (Fig. 5f), while the Cl contents remained nearly the same in these states. These observations further demonstrate that the storage ions are Al^{3+} ions rather than $AlCl_4^-$ ions. Additionally, Co and O are uniformly distributed across the nanosheets, verifying the good mechanical stability of the Co_3O_{4-x} cathode. According to the above analysis, the reaction during the discharging and charging process can be described as follows, eqn (1) and (2):

$$\text{Cathode: } Co_3O_{4-x} + lAl^{3+} + 3le^- \rightleftharpoons Al_lCo_mO_{4-x} + (3-m)\,Co \quad (1)$$

$$\text{Anode: } Al + 7AlCl_4^- - 3e^- \rightleftharpoons 4Al_2Cl_7^- \quad (2)$$

To further understand the roles of oxygen vacancies for enhancing the electrochemical performance, pseudocapacitive analysis, electrochemical impedance spectroscopic (EIS) measurements, and density functional theory (DFT) were conducted. First, the CV tests were carried out at different scan rates from 0.5 to 2.5 mV s^{-1} to provide more in-depth insight into the charge storage mechanism of these products (Fig. 6a and c). The relationship between the scan rates (v) and the corresponding peak currents (i) can be calculated to reflect the diffusion-controlled behavior and surface capacitive-controlled behavior. This relationship is exhibited by the equation $i = av^b$, where $b = 0.5$ and 1.0 respectively means the diffusion-controlled behavior and capacitive-controlled behavior.[14,56] For Co_3O_4 nanosheets, the b value is 0.309 for the cathodic peak and 0.710 for the anodic peak (inset of Fig. 6c), indicating that Al-diffusion kinetics is mainly diffusion controlled. However, for Co_3O_{4-x} nanosheets, the b value of the two peaks is 0.695 and 0.818 (Fig. 6b), respectively, suggesting the improvement in the capacitive process, which contributes to faster ion transfer and reaction kinetics of the Co_3O_{4-x} electrode.[57] Furthermore, the capacitive contribution can be determined from the equation $i(V) = k_1v + k_2v^{1/2}$, where $i(V)$ represents the current obtained under a given voltage V, and k_1v and k_2v correspond to the current contributions from the diffusion-controlled and capacitive-controlled behavior, respectively.[35] As shown in Fig. 6d, the calculated capacitive contributions of the Co_3O_{4-x} nanosheets are 41.9, 52.7, 58.9, 65.7, and 73.5% at 0.5, 1.0, 1.5, 2.0, and 2.5 mV s^{-1}, respectively, which are higher than those of Co_3O_4 nanosheets, indicating that the introduction of oxygen defects can boost charge storage and thus contribute to good rate performance.[58] EIS spectra were obtained in the frequency window of 100 kHz to 10 mHz to further confirm the fast charge transfer and ionic diffusion kinetics. As shown in the enlarged EIS curves in the inset of Fig. 6e, the charge transfer resistance (R_{ct}) values for Co_3O_{4-x} and Co_3O_4 porous nanosheets are all less than 5 Ω, reflecting the high electron conductivity of these cathodes. Moreover, the straight line in the low frequency can reflect the ion diffusion kinetics, and the steeper one indicates faster ion diffusion ability.[59] The Al^{3+} diffusion ability can be further reflected by the slope of the straight line in the low frequency region. It can be calculated by the following formulas: $\omega = 2\pi f$ and $Z = R + \sigma\omega^{-1/2}$.[60] Here, ω, f, and Z are the angular frequency, test frequency, and real part of impedance,

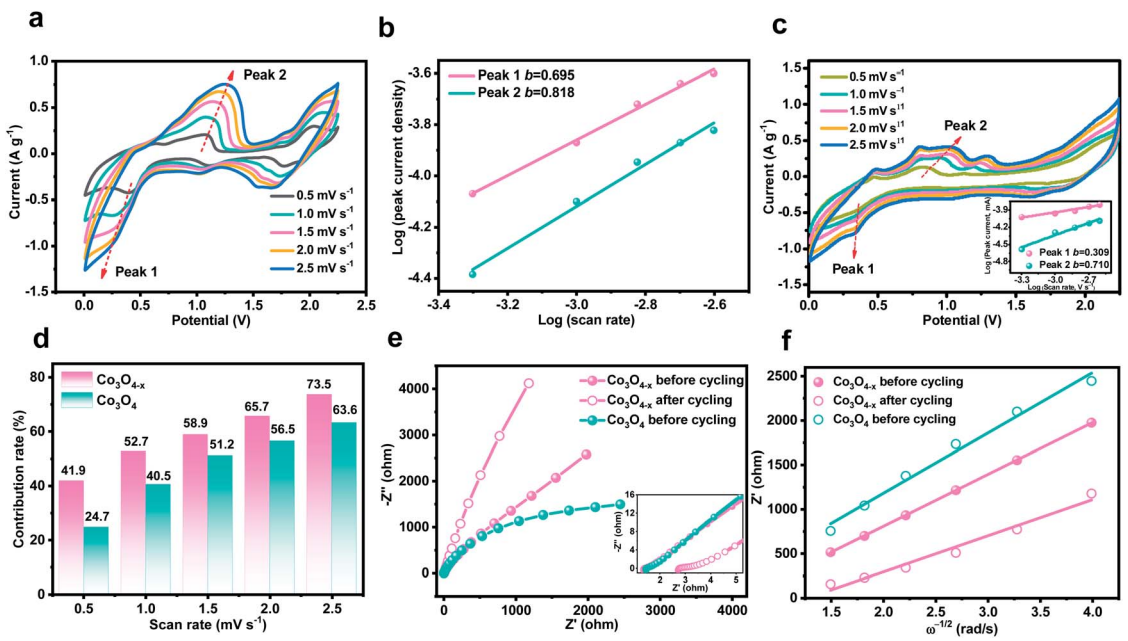

Fig. 6 (a) CV curves at different scan rates from 0.5 to 2.5 mV s^{-1} of Co_3O_{4-x}. (b) Linear relationship between log(scan rate) and log(peak current density). (c) CV curves at different scan rates from 0.5 to 2.5 mV s^{-1} of Co_3O_4. The inset is the linear relationship between log(scan rate) and log(peak current density). (d) Contribution ratios of capacitive capacity at various scan rates. (e and f) EIS and relationship between real impedance with low frequency of Co_3O_{4-x} and Co_3O_4, respectively.

respectively. And, σ is Warburg coefficient, the linear slope derived from the relationship between the real part of the impedance and low frequency; a smaller σ indicates faster ion diffusion rate (Fig. 6f). Before cycling, the Co_3O_{4-x} nanosheets show a smaller slope of the linear tendency than that of Co_3O_4 nanosheets, verifying that the oxygen vacancies can boost Al^{3+} ion diffusion.[60] Besides, the slope of Co_3O_{4-x} nanosheets decreases after 50 cycles, corresponding to the enhanced Al^{3+} diffusion rate. It can be inferred that the initial cycling process activates the electrode, enhancing the Al^{3+} diffusion ability.

DFT calculations were conducted to study the effect of oxygen defects on the electrode performance. Fig. 7a and b show the optimized structures of Co_3O_4 and Co_3O_{4-x} with adsorbed Al^{3+}, respectively. The perfect Co_3O_4 shows stronger Al^{3+} adsorption with a lower adsorption free energy of around −4.2 eV, indicating that it is thermodynamically less favorable for the subsequent Al^{3+} desorption. *Via* introduction of oxygen vacancies, Co_3O_{4-x} has a thermoneutral Gibbs free energy of Al^{3+} adsorption (−3.45 eV). It suggests that Co_3O_{4-x} benefits the fast release of Al^{3+}, and thus favors the reversible adsorption/desorption process.[40] The diffusion processes of Al^{3+} ions in Co_3O_{4-x} and Co_3O_4 were simulated by the CI-NEB method. Fig. 7c and S10† exhibit the possible Al^{3+} migration paths in Co_3O_{4-x} and Co_3O_4, respectively. As observed from the calculated energy curves (Fig. 7d), the Al^{3+} diffusion energy barrier of Co_3O_{4-x} (2.37 eV) is lower than that in Co_3O_4 (3.12 eV), indicating that the oxygen vacancies can facilitate the Al^{3+} diffusion. In addition, the thermodynamic calculations of the electrochemical reactions between Al^{3+} and Co_3O_{4-x} (Co_3O_4) were further conducted. According to the obtained conversion reaction mechanism, the electrochemical reaction process can be divided into two parts: one Al(III) ion replaces one hexacoordinated Co ion (Co (H)) (defined as reaction 1) and two Al(III) ions and one vacancy replace three tetracoordinate Co ions (Co (T)) (defined as reaction 2). Reaction 2 may also proceed stepwise by replacing one Co (H) with one Al(III) ion and two Co (H) with one Al(III) ion and a vacancy, respectively. As shown in Fig. 7e–i, the formation energies of reaction 2 for Co_3O_4 and Co_3O_{4-x} are −9.63 and −10.08 eV, respectively, which are much lower than those in reaction 1 (Co_3O_4: −5.67 eV; Co_3O_{4-x}: −4.93 eV), revealing that reaction 2 involving the participation of vacancies is more facile. Moreover, Co_3O_{4-x} shows lower formation energy (−10.08 eV) than Co_3O_4 (−9.63 eV) in reaction 2. This suggests an effortless Al^{3+} insertion into Co_3O_{4-x}, explaining its higher Al^{3+} ion storage capacity.

The structural stability of the Co_3O_{4-x} electrode after cycling was characterized by SEM and TEM. After prolonged cycles at the current density of 1 A g^{-1}, Co_3O_{4-x} nanosheets still retain the porous layer morphology and distinct lattices without structural damage (Fig. S11a–d†). Additionally, the

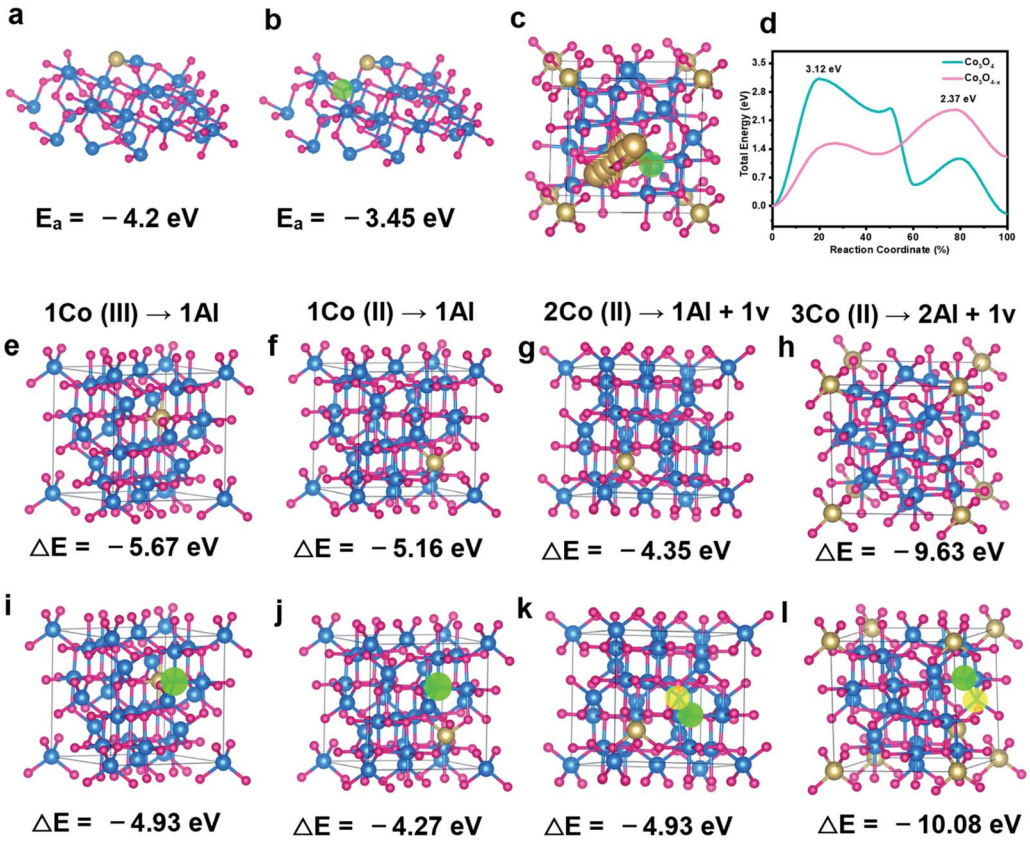

Fig. 7 The structural geometry of the Al^{3+} adsorption on (a) Co_3O_4 and (b) Co_3O_{4-x}. (c) Migration path of Al^{3+} in Co_3O_{4-x}. (d) Calculated diffusion barrier curves of Al^{3+} in Co_3O_{4-x} and Co_3O_4. The formation energies of the possible conversion reactions in (e–h) Co_3O_4 and (i–l) Co_3O_{4-x}. The oxygen vacancy and formed cobalt vacancy are marked with green and yellow circles, respectively.

corresponding STEM-EDX elemental mapping images of the cycled Co_3O_{4-x} electrode (Fig. S11e†) reveal that each element is evenly distributed, further confirming its remarkable reaction reversibility and desirable structural stability during the repeated Al^{3+} intercalation/deintercalation process.

Experimental section

Synthesis of Co-MOF nanosheets

0.616 g of 2-methylimidazole (2-MIM) and 0.546 g of $Co(NO_3)_2 \cdot 6H_2O$ were added separately into 7 mL of methanol, and the formed solutions were named solution A and solution B, respectively. Then, solution B was poured into solution A under mechanical stirring followed by sonication for 15 min to form solution C. Another solution B was then poured into the obtained solution C. The mixture was transferred to 50 mL teflon-lined stainless-steel autoclaves and kept at 120 °C for 60 min. The obtained Co-MOF product was washed with methanol three times and dried under vacuum at 60 °C overnight.

Synthesis of Co_3O_{4-x} porous nanosheets

The as-prepared Co-MOF precursor was calcined in air at 400 °C for 60 min, the obtained product was named Co_3O_4 porous nanosheets. Then 100 mg pristine Co_3O_4 nanosheets were immersed in 100 mL $NaBH_4$ solution (0.1 M) for 60 min. After the reduction reaction, the dark product was thoroughly washed with deionized water and ethanol several times and dried under vacuum at 60 °C overnight.

Materials characterization

Scanning electron microscopy (SEM) images were obtained using a JEOL 7500FA microscope (Tokyo, Japan). Transmission electron microscopy (TEM) images, scanning TEM with energy dispersive X-ray spectroscopy (STEM-EDX) elemental mapping images were obtained using a JEOL 2011 F (Tokyo, Japan) coupled with an EDX spectrometer operated at 200 kV. The structures were studied using powder X-ray diffraction (XRD) patterns collected on a Bruker AXS D8 Advance powder X-ray diffractometer with monochromatic Cu Kα radiation. The element valences were revealed by X-ray photoelectron spectroscopy (XPS; PerkinElmer PHI 5000C ESCA). The nitrogen adsorption/desorption isotherms were obtained at liquid nitrogen temperature using a Quadrasorb SI-MP analyzer. Raman spectra were collected using a Renishaw in *Via* micro-Raman spectrometer with a 532 nm excitation laser. Electron spin resonance tests (EPR, A300) were carried out in the X-band with a 5.00 G modulation amplitude.

Electrochemical measurements

The cathode was fabricated by mixing active materials, super P acetylene black, and polyvinylidene fluoride (PVDF) in *N*-methyl-2-pyrrolidinone (NMP) solvent thoroughly with a mass ratio of 7 : 2 : 1. The slurry was cast on Mo foil and dried in a vacuum oven at 80 °C overnight. Before preparation of the electrolyte, 1-ethyl-3-methylimidazolium chloride ([EMIm]Cl) was dried at 130 °C under vacuum for 24 h. Then, the ionic liquid electrolyte was obtained *via* mixing [EMIm]Cl and anhydrous $AlCl_3$ with a molar ratio of 1 : 1.3 in an Ar-filled glove box (<0.1 ppm of H_2O and O_2). The Swagelok-type cell was assembled with the as-prepared cathode, aluminum metal foil (99.99%) anode, paper glass fiber (GF/D) separator, and the ion liquid electrolyte. Galvanostatic charge/discharge tests were carried out on a battery testing system (Land-CT2001A) with a suitable voltage window of 0.01–2.25 V at room temperature. Cyclic voltammetry (CV) measurements and electrochemical impedance spectroscopy (EIS) tests performed in the frequency window of 100 kHz–10 mHz were conducted on a CHI 660D electrochemical workstation.

Computational methods

All density functional theory (DFT) calculations were performed with Vienna *ab initio* Simulation Package (VASP).[61–63] The generalized gradient approximation (GGA) with a Perdew–Burke–Ernzerhof (PBE) exchange correlation functional and projector-augmented wave (PAW) method were used.[64] During the optimization process, the structures were relaxed until the forces and total energy on all atoms were converged to less than 0.05 eV $Å^{-1}$ and 1×10^{-5} eV. A cut-off energy of 600 eV and Gamma centered $2 \times 2 \times 2$ k-point mesh were set for all calculations. Spin-polarization was also considered in all calculations. To analyze the effect of oxygen vacancy in Co_3O_{4-x}, a cubic supercell of $a = b = c = 7.96$ Å with 24 Co atoms, 32 O atoms was set as the pristine structure, and another supercell with one O atom was removed as the modified structure. The electrochemical reaction between aluminum and the cathode is described as: $l\mathrm{Al} + Co_3O_{4-x} \rightarrow Al_lCo_mO_{4-x} + (3 - m)$ Co. The model of $Al_lCo_mO_{4-x}$ was simply set by substituting Al atoms and cation vacancies for Co atoms. And the energy change of the reaction is defined as: $\Delta E = E_{sub} + lE_{Co} - E_{matrix} - mE_{Al}$. The kinetic process of aluminum transport in the matrix was simulated by the Climbing Image Nudged Elastic Band (CI-NEB) method.[65,66] 4 images were inserted between the initial and final structures as transition states.

Conclusion

In summary, a facile strategy is developed to fabricate oxygen-deficient Co_3O_{4-x} porous nanosheets as an advanced Al^{3+} ion storage host. Benefiting from the oxygen defects and the ultra-thin porous structure, Co_3O_{4-x} displays satisfactory pseudocapacitive behavior, which enables good rate capability. Moreover, the DFT calculations reveal reversible Al^{3+} adsorption/desorption together with favorable Al^{3+} incorporation and diffusion capability of Co_3O_{4-x}, explaining the desirable reversibility, high capacity, and fast Al^{3+} release/storage of this novel cathode. As expected, the Co_3O_{4-x} porous nanosheets exhibit a high reversible capacity of 442.3 mA h g^{-1} at a high current density of 1.0 A g^{-1} and still retain 104.2 mA h g^{-1} after 1800 cycles, outperforming other reported oxide cathode materials. *Ex situ* tests uncover the robust structural integrity which can withstand continuous Al^{3+}-ion insertion/extraction

as well as the conversion reaction mechanism. This work highlights the importance of the relationship between structural defects and Al^{3+} storage performance, inspiring a pathway of structural engineering strategy towards advanced AIB cathodes.

Author contributions

Jiening Zheng: conceptualization, data curation, formal analysis, investigation, methodology, writing – original draft, writing – review & editing. Tian Xu: formal analysis. Guanglin Xia: supervision. Xuebin Yu: funding acquisition, project administration, resources, supervision, validation, writing –review & editing.

Conflicts of interest

There are no conflicts to declare.

Acknowledgements

This work was partially supported by the National Science Fund for Distinguished Young Scholars (51625102), the National Natural Science Foundation of China (51971065), and the Innovation Program of Shanghai Municipal Education Commission (2019-01-07-00-07-E00028).

Notes and references

1 A. Magasinski, P. Dixon, B. Hertzberg, A. Kvit, J. Ayala and G. Yushin, *Nat. Mater.*, 2010, **9**, 353–358.
2 K. Kang, Y. S. Meng, J. Bréger, C. P. Grey and G. Ceder, *Science*, 2006, **311**, 977–980.
3 J. W. Choi and D. Aurbach, *Nat. Rev. Mater.*, 2016, **1**, 16013.
4 G. Harper, R. Sommerville, E. Kendrick, L. Driscoll, P. Slater, R. Stolkin, A. Walton, P. Christensen, O. Heidrich, S. Lambert, A. Abbott, K. Ryder, L. Gaines and P. Anderson, *Nature*, 2019, **575**, 75–86.
5 M. Jiang, C. Fu, P. Meng, J. Ren, J. Wang, J. Bu, A. Dong, J. Zhang, W. Xiao and B. Sun, *Adv.Mater.*, 2022, **34**, 2102026.
6 M.-C. Lin, M. Gong, B. Lu, Y. Wu, D.-Y. Wang, M. Guan, M. Angell, C. Chen, J. Yang, B.-J. Hwang and H. Dai, *Nature*, 2015, **520**, 324–328.
7 Z. Liu, J. Wang, H. Ding, S. Chen, X. Yu and B. Lu, *ACS Nano*, 2018, **12**, 8456–8466.
8 Y. Wu, M. Gong, M.-C. Lin, C. Yuan, M. Angell, L. Huang, D.-Y. Wang, X. Zhang, J. Yang, B.-J. Hwang and H. Dai, *Adv.Mater.*, 2016, **28**, 9218–9222.
9 D.-Y. Wang, C.-Y. Wei, M.-C. Lin, C.-J. Pan, H.-L. Chou, H.-A. Chen, M. Gong, Y. Wu, C. Yuan, M. Angell, Y.-J. Hsieh, Y.-H. Chen, C.-Y. Wen, C.-W. Chen, B.-J. Hwang, C.-C. Chen and H. Dai, *Nat. Commun.*, 2017, **8**, 14283.
10 H. Chen, C. Chen, Y. Liu, X. Zhao, N. Ananth, B. Zheng, L. Peng, T. Huang, W. Gao and C. Gao, *Adv. Energy Mater.*, 2017, **7**, 1700051.
11 L. Zhang, L. Chen, H. Luo, X. Zhou and Z. Liu, *Adv. Energy Mater.*, 2017, **7**, 1700034.
12 Q. Zhang, L. Wang, J. Wang, C. Xing, J. Ge, L. Fan, Z. Liu, X. Lu, M. Wu, X. Yu, H. Zhang and B. Lu, *Energy Stor. Mater.*, 2018, **15**, 361–367.
13 Y. Kong, C. Tang, X. Huang, A. K. Nanjundan, J. Zou, A. Du and C. Yu, *Adv. Funct. Mater.*, 2021, **31**, 2010569.
14 D.-J. Yoo, M. Heeney, F. Glöcklhofer and J. W. Choi, *Nat. Commun.*, 2021, **12**, 2386.
15 T. Koketsu, J. Ma, B. J. Morgan, M. Body, C. Legein, W. Dachraoui, M. Giannini, A. Demortière, M. Salanne, F. Dardoize, H. Groult, O. J. Borkiewicz, K. W. Chapman, P. Strasser and D. Dambournet, *Nat. Mater.*, 2017, **16**, 1142–1148.
16 Y. Ai, S.-C. Wu, K. Wang, T.-Y. Yang, M. Liu, H.-J. Liao, J. Sun, J.-H. Chen, S.-Y. Tang, D. C. Wu, T.-Y. Su, Y.-C. Wang, H.-C. Chen, S. Zhang, W.-W. Liu, Y.-Z. Chen, L. Lee, J.-H. He, Z. M. Wang and Y.-L. Chueh, *ACS Nano*, 2020, **14**, 8539–8550.
17 S. Lu, M. Wang, F. Guo, J. Tu, A. Lv, Y. Chen and S. Jiao, *Chem. Eng. J.*, 2020, **389**, 124370.
18 D.-S. Liu, D.-H. Liu, B.-H. Hou, Y.-Y. Wang, J.-Z. Guo, Q.-L. Ning and X.-L. Wu, *Electrochim. Acta*, 2018, **264**, 292–300.
19 R. Sun, Z. Qin, Z. Li, H. Fan and S. Lu, *Dalton Trans.*, 2020, **49**, 14237–14242.
20 Y. Heng, Z. Gu, J. Guo and X. Wu, *Acta Phys.-Chim. Sin.*, 2021, **37**, 2005013.
21 R. Sun, S. Dong, F. Xu, Z. Li, C. Wang, S. Lu and H. Fan, *Dalton Trans.*, 2022, **51**, 7607–7612.
22 C. Hou, Y. Hou, Y. Fan, Y. Zhai, Y. Wang, Z. Sun, R. Fan, F. Dang and J. Wang, *J. Mater. Chem. A*, 2018, **6**, 6967–6976.
23 J. Liu, Z. Li, X. Huo and J. Li, *J. Power Sources*, 2019, **422**, 49–56.
24 D. Wang, Y. Yu, H. He, J. Wang, W. Zhou and H. D. Abruña, *ACS Nano*, 2015, **9**, 1775–1781.
25 C. Li, S. Dong, P. Wang, C. Wang and L. Yin, *Adv. Energy Mater.*, 2019, **9**, 1902352.
26 F. Wu, H. Yang, Y. Bai and C. Wu, *Adv. Mater.*, 2019, **31**, 1806510.
27 W. Kaveevivitchai, A. Huq, S. Wang, M. J. Park and A. Manthiram, *Small*, 2017, **13**, 1701296.
28 T. Xiong, Y. Zhang, W. S. V. Lee and J. Xue, *Adv. Energy Mater.*, 2020, **10**, 2001769.
29 X. Yang, Y. Luo, J. Li, H. Wang, Y. Song, J. Li and Z. Guo, *Adv. Funct. Mater.*, 2022, **32**, 2112169.
30 G. Wang, Y. Yang, D. Han and Y. Li, *Nano Today*, 2017, **13**, 23–39.
31 Y. Li, J. Qian, M. Zhang, S. Wang, Z. Wang, M. Li, Y. Bai, Q. An, H. Xu, F. Wu, L. Mai and C. Wu, *Adv. Mater.*, 2020, **32**, 2005802.
32 K. Xiang, Z. Xu, T. Qu, Z. Tian, Y. Zhang, Y. Wang, M. Xie, X. Guo, W. Ding and X. Guo, *Chem. Commun.*, 2017, **53**, 12410–12413.
33 Y. M. Chen, L. Yu and X. W. Lou, *Angew. Chem., Int. Ed.*, 2016, **55**, 5990–5993.

34 J. Wang, Y. Xia, Y. Dong, R. Chen, L. Xiang and S. Komarneni, *Appl. Catal. B Environ.*, 2016, **192**, 8–16.
35 J. Lin, C. Zeng, X. Lin, C. Xu, X. Xu and Y. Luo, *ACS Nano*, 2021, **15**, 4594–4607.
36 H. Sun, Y. Zhao, K. Mølhave, M. Zhang and J. Zhang, *Nanoscale*, 2017, **9**, 14431–14441.
37 Z. Cai, Y. Bi, E. Hu, W. Liu, N. Dwarica, Y. Tian, X. Li, Y. Kuang, Y. Li, X.-Q. Yang, H. Wang and X. Sun, *Adv. Energy Mater.*, 2018, **8**, 1701694.
38 H. Luo, B. Wang, C. Wang, F. Wu, F. Jin, B. Cong, Y. Ning, Y. Zhou, D. Wang, H. Liu and S. Dou, *Energy Stor. Mater.*, 2020, **33**, 390–398.
39 Q. Tan, X. Li, B. Zhang, X. Chen, Y. Tian, H. Wan, L. Zhang, L. Miao, C. Wang, Y. Gan, J. Jiang, Y. Wang and H. Wang, *Adv. Energy Mater.*, 2020, **10**, 2001050.
40 M. Liao, J. Wang, L. Ye, H. Sun, Y. Wen, C. Wang, X. Sun, B. Wang and H. Peng, *Angew. Chem.*, 2020, **59**, 2273–2278.
41 Y. Li, Q. Zhang, Y. Yuan, H. Liu, C. Yang, Z. Lin and J. Lu, *Adv. Energy Mater.*, 2020, **10**, 2000717.
42 H. Li, H. Yang, Z. Sun, Y. Shi, H.-M. Cheng and F. Li, *Nano Energy*, 2019, **56**, 100–108.
43 X. Zhu, Z. Cao, W. Wang, H. Li, J. Dong, S. Gao, D. Xu, L. Li, J. Shen and M. Ye, *ACS Nano*, 2021, **15**, 2971–2983.
44 A. VahidMohammadi, A. Hadjikhani, S. Shahbazmohamadi and M. Beidaghi, *ACS Nano*, 2017, **11**, 11135–11144.
45 S. Wang, S. Jiao, J. Wang, H.-S. Chen, D. Tian, H. Lei and D.-N. Fang, *ACS Nano*, 2017, **11**, 469–477.
46 L. Wu, R. Sun, F. Xiong, C. Pei, K. Han, C. Peng, Y. Fan, W. Yang, Q. An and L. Mai, *Phys. Chem. Chem. Phys.*, 2018, **20**, 22563–22568.
47 X. Zhang, G. Zhang, S. Wang, S. Li and S. Jiao, *J. Mater. Chem. A*, 2018, **6**, 3084–3090.
48 J. Tu, H. Lei, Z. Yu and S. Jiao, *Chem. Commun.*, 2018, **54**, 1343–1346.
49 X. Xiao, M. Wang, J. Tu, Y. Luo and S. Jiao, *ACS Sustain. Chem. Eng.*, 2019, **7**, 16200–16208.
50 L. Wang, H. Lin, W. Kong, Y. Hu, R. Chen, P. Zhao, M. Shokouhimehr, X. L. Zhang, Z. Tie and Z. Jin, *Nanoscale*, 2020, **12**, 12531–12540.
51 N. Zhu, F. Wu, Z. Wang, L. Ling, H. Yang, Y. Gao, S. Guo, l. Suo, H. Li, H. Xu, Y. Bai and C. Wu, *J. Energy Chem.*, 2020, **51**, 72–80.
52 A. M. Diem, J. Bill and Z. Burghard, *ACS Appl. Energy Mater.*, 2020, **3**, 4033–4042.
53 P. Almodóvar, D. A. Giraldo, J. Chancón, I. Álvarez-Serrano and M. L. López, *ChemElectroChem*, 2020, **7**, 2102–2106.
54 J. Tu, M. Wang, Y. Luo and S. Jiao, *ACS Sustain. Chem. Eng.*, 2020, **8**, 2416–2422.
55 P. Almodóvar, D. Giraldo, C. Díaz-Guerra, J. Ramírez-Castellanos, J. M. González Calbet, J. Chacón and M. L. López, *J. Power Sources*, 2021, **516**, 230656.
56 W. Liu, S. Ju and X. Yu, *ACS Nano*, 2020, **14**, 974–984.
57 N. Wang, Z. Bai, Y. Qian and J. Yang, *Adv. Mater.*, 2016, **28**, 4126–4133.
58 Y. Zhang, P. Chen, Q. Wang, Q. Wang, K. Zhu, K. Ye, G. Wang, D. Cao, J. Yan and Q. Zhang, *Adv. Energy Mater.*, 2021, **11**, 2101712.
59 J. Zheng, S. Ju, G. Xia, H. Pan and X. Yu, *ACS Appl. Mater. Interfaces*, 2022, **14**, 8076–8085.
60 B. Wang, J. Yan, Y. Zhang, M. Ye, Y. Yang and C. C. Li, *Adv. Funct. Mater.*, 2021, **31**, 2102827.
61 G. Kresse and J. Hafner, *Phys. Rev. B: Condens. Matter Mater. Phys.*, 1993, **47**, 558–561.
62 G. Kresse and J. Furthmüller, *Comput. Mater. Sci.*, 1996, **6**, 15–50.
63 G. Kresse and J. Furthmüller, *Phys. Rev. B: Condens. Matter Mater. Phys.*, 1996, **54**, 11169–11186.
64 G. Kresse and D. Joubert, *Phys. Rev. B: Condens. Matter Mater. Phys.*, 1999, **59**, 1758–1775.
65 G. Henkelman, B. P. Uberuaga and H. Jónsson, *J. Chem. Phys.*, 2000, **113**, 9901–9904.
66 G. Henkelman and H. Jónsson, *J. Chem. Phys.*, 2000, **113**, 9978–9985.

